Supporting Information

Synergy of the catalytic activation on Ni and CeO_2-TiO_2 / $Ce_2Ti_2O_7$ stoichiometric redox cycle for dramatically enhanced solar fuel production

Chongyan Ruan,‡[ac] Zheng-Qing Huang,‡[b] Jian Lin,[a] Lin Li,[a] Xiaoyan Liu,[a] Ming Tian,[a] Chuande Huang,[a] Chun-Ran Chang,*[b] Jun Li[d] and Xiaodong Wang*[a]

[a] Dalian Institute of Chemical Physics, Chinese Academy of Sciences, Dalian 116023, China

[b] Shaanxi Key Laboratory of Energy Chemical Process Intensification, School of Chemical Engineering and Technology, Xi'an Jiaotong University, Xi'an 710049, China

[c] University of Chinese Academy of Sciences, Beijing, 100049, China

[d] Department of Chemistry and Key Laboratory of Organic Optoelectronics & Molecular Engineering of Ministry of Education, Tsinghua University, Beijing, 100084, China

‡ Co-first authors

***Corresponding Authors**: xdwang@dicp.ac.cn; changcr@mail.xjtu.edu.cn

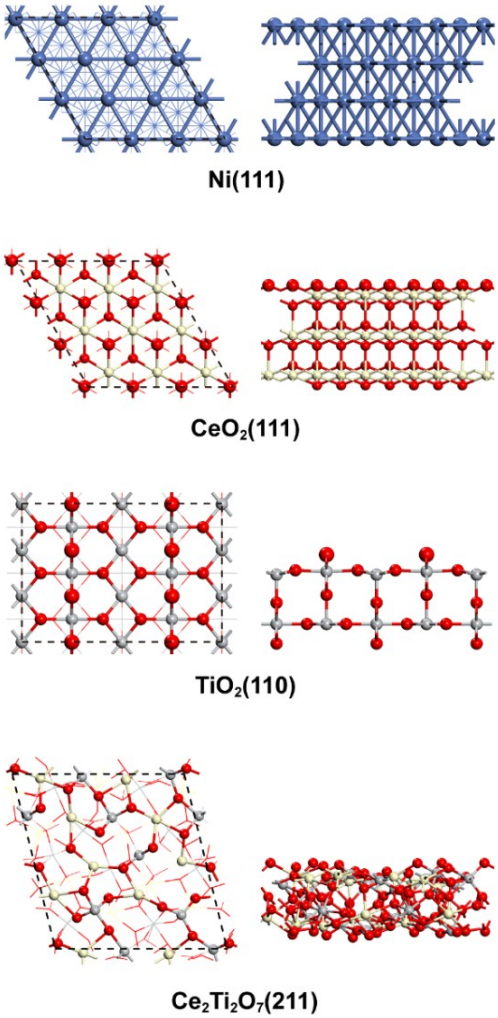

Fig. S1 Top (left) and side (right) view of optimized Ni(111), CeO_2(111), TiO_2(110) and $Ce_2Ti_2O_7$(211) surfaces. These surface models are constructed based on our XRD and HRTEM characterizations.

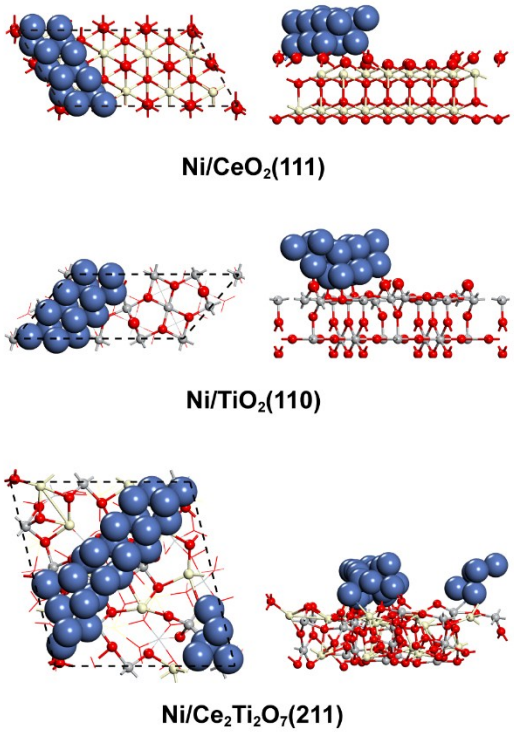

Fig. S2 Top (left) and side (right) view of optimized Ni/CeO_2(111), Ni/TiO_2(110), and Ni/$Ce_2Ti_2O_7$(211) structures.

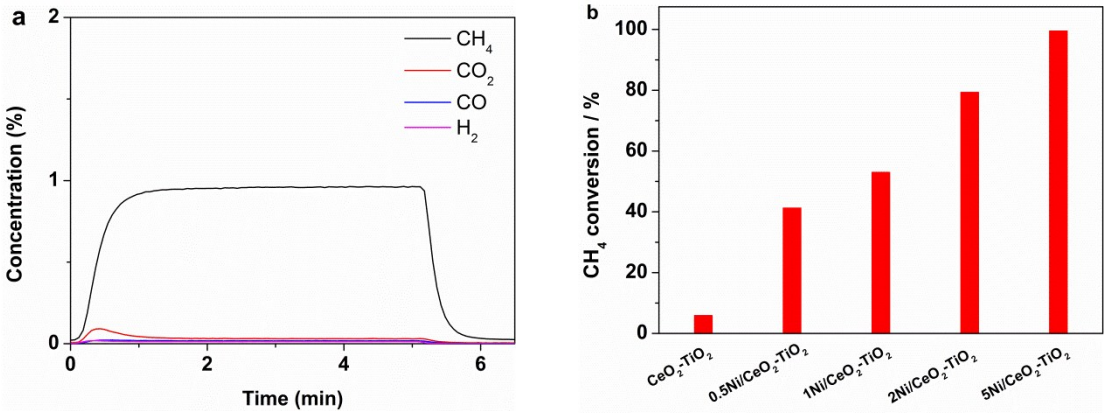

Fig. S3 (a) Temporal gaseous products concentrations for CeO_2-TiO_2 during the CH_4 reduction half cycle of the isothermal MDR-STWS process at 900 °C. (b) Average CH_4 conversion for CeO_2-TiO_2 with different Ni loadings (0, 0.5, 1, 2, and 5 wt%) during the CH_4 reduction half cycle of the isothermal MDR-STWS process.

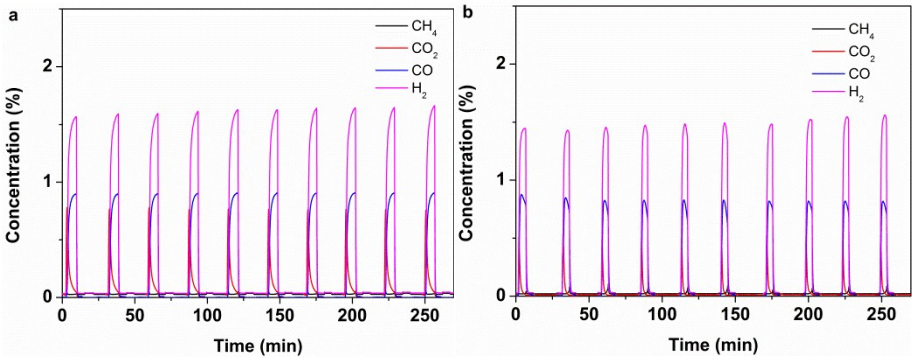

Fig. S4 Temporal gaseous products concentrations for 5Ni/CeO_2-TiO_2 during the CH_4 reduction half cycle of the isothermal (a) MDR-STCDS and (b) MDR-STWS processes at 900 °C over 10 redox cycles.

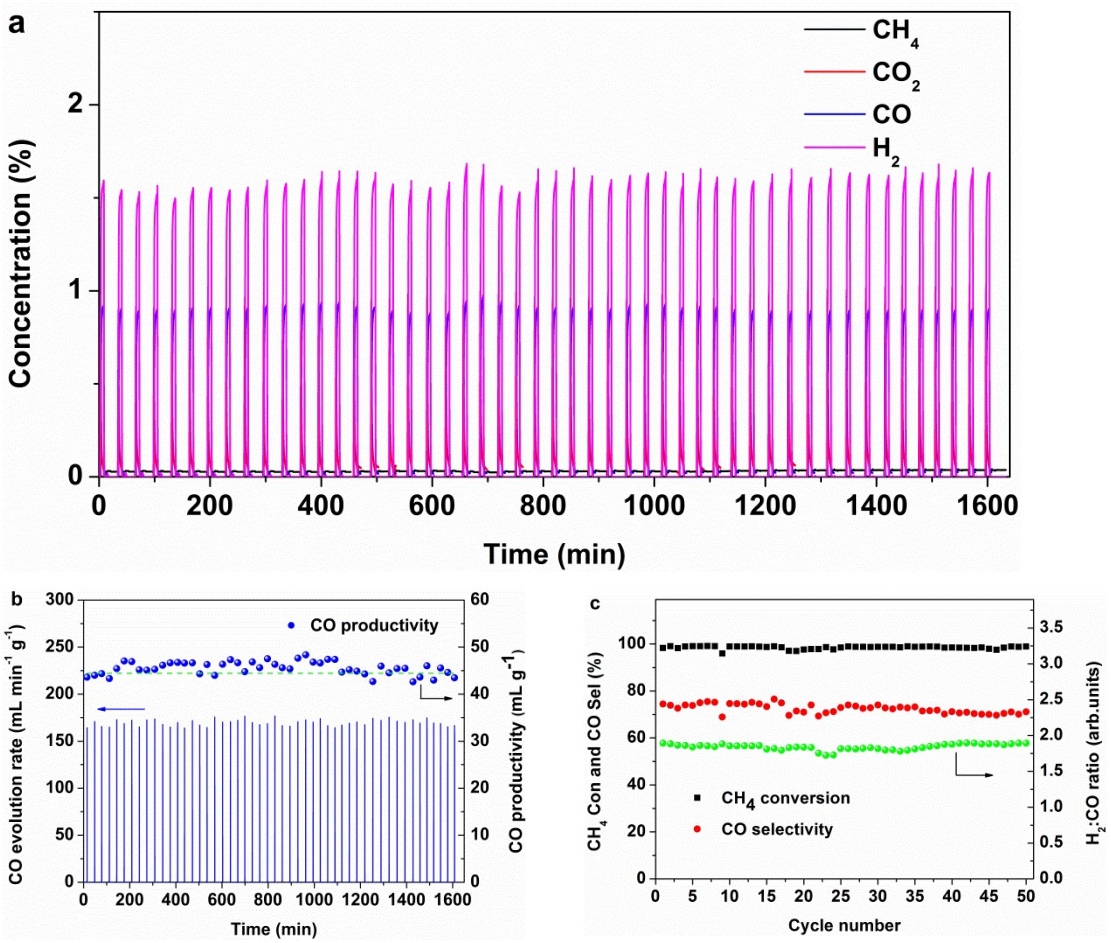

Fig. S5 (a) Temporal gaseous products concentrations for 5Ni/CeO_2-TiO_2 during the CH_4 reduction half cycles of the isothermal MDR-STCDS process at 900 °C over 50 redox cycles. (b) The corresponding transient CO evolution rates for 5Ni/CeO_2-TiO_2 during the CO_2 splitting half cycles of the isothermal MDR-STCDS process over 50 redox cycles. The dashed horizontal line gives the theoretical CO yield of 44.5 mL CO g^{-1} for 5Ni/CeO_2-TiO_2 assuming a full reduction to Ce^{3+}. (c) Average CH_4 conversion, CO selectivity and H_2/CO ratio for 5Ni/CeO_2-TiO_2 during the CH_4 reduction half cycle of the isothermal MDR-STCDS process over 50 redox cycles.

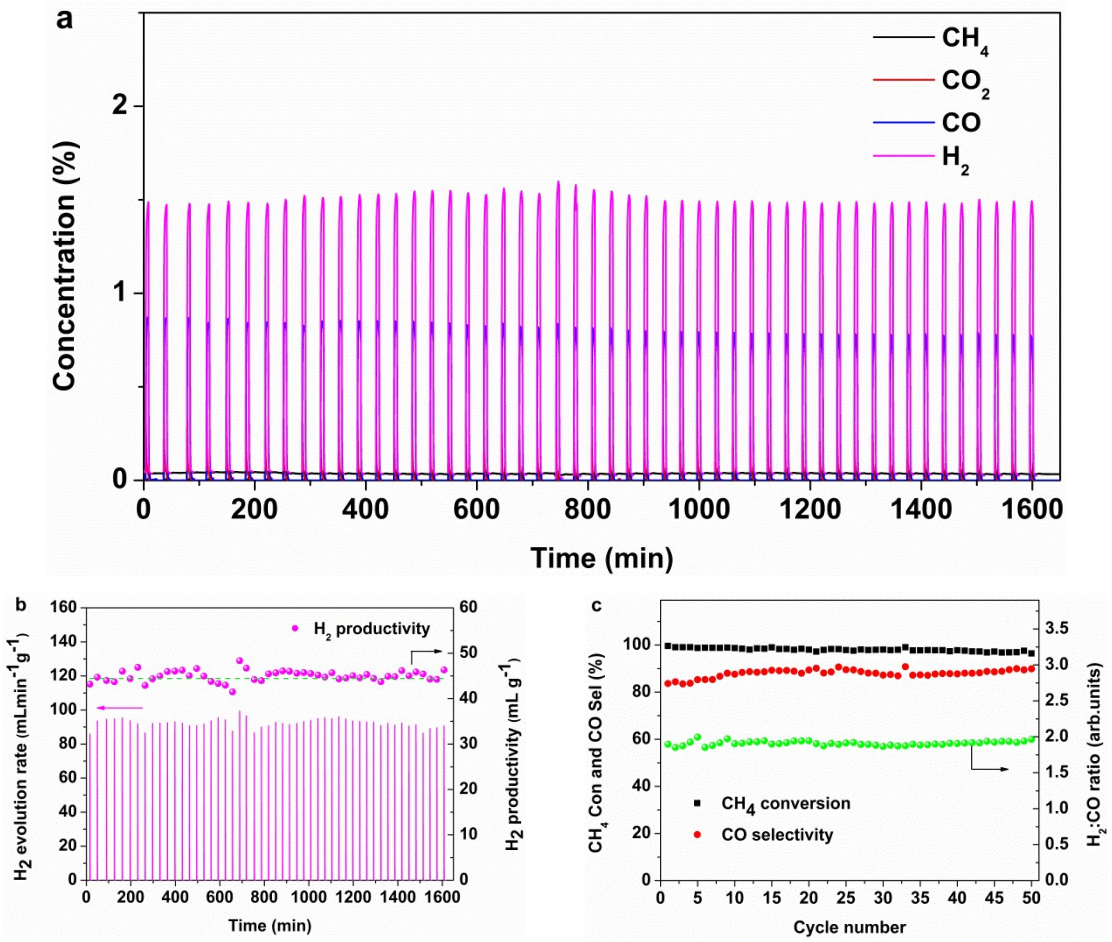

Fig. S6 (a) Temporal gaseous products concentrations for 5Ni/CeO_2-TiO_2 during the CH_4 reduction half cycles of the isothermal MDR-STWS process at 900 °C over 50 redox cycles. (b) The corresponding transient H_2 evolution rates for 5Ni/CeO_2-TiO_2 during the H_2O splitting half cycles of the isothermal MDR-STWS process over 50 redox cycles. The dashed horizontal line gives the theoretical H_2 yield of 44.5 mL H_2 g^{-1} for 5Ni/CeO_2-TiO_2 assuming a full reduction to Ce^{3+}. (c) Average CH_4 conversion, CO selectivity and H_2/CO ratio for 5Ni/CeO_2-TiO_2 during the CH_4 reduction half cycle of the isothermal MDR-STWS process over 50 redox cycles.

Fig. S5 and Fig. S6 show catalytic performance of 5Ni/CeO_2-TiO_2 for the cyclic MDR-STCDS and MDR-STWS redox processes at 900 °C. The instantaneous gaseous products concentrations for 5Ni/CeO_2-TiO_2 during the CH_4 reduction half cycle of the isothermal MDR-STCDS and MDR-STWS processes were relatively constant among 50 redox cycles (within experimental error), as shown in Fig. S5a and Fig. S6a, confirming that 5Ni/CeO_2-TiO_2 could be reduced with CH_4 repeatedly with high reproducibility. Meanwhile, reproducible kinetic curves of CO and H_2 evolution rates were observed during the CO_2 and H_2O splitting half cycles (Fig. S5b and Fig. S6b). The CO (Fig. S5b) or H_2 (Fig. S6b) productivity, estimated by integrating the corresponding transient CO or H_2 evolution rate with respect to time, stayed relatively constant over the course of 50 repetitive cycles, which was comparable to theoretically expected value (44.5 mL CO/H_2 g^{-1} assuming a full reduction to Ce^{3+}) stoichiometrically available for complete oxidation of Ce^{3+} to Ce^{4+}. The corresponding catalytic performance of 5Ni/CeO_2-TiO_2 during CH_4 reduction is summarized in Fig. S5c and Fig. S6c. Negligible change was observed in term of CH_4 conversion (CH_4 Con), H_2/CO ratio, as well as the CO selectivity (CO Sele). Specifically, essentially complete conversions of CH_4 were achieved for both processes over entire 50 redox cycles, with H_2 : CO ratios stabilized at ~1.8 (Fig. S5c) and ~1.9 (Fig. S6c). The CO selectivity for 5Ni/CeO_2-TiO_2 in the isothermal MDR-STCDS and MDR-STWS processes remained between 70–76% and 83–91%, respectively. Therefore, it was confirmed that the 5Ni/CeO_2-TiO_2 redox catalyst possesses excellent recyclability over cyclic redox processes.

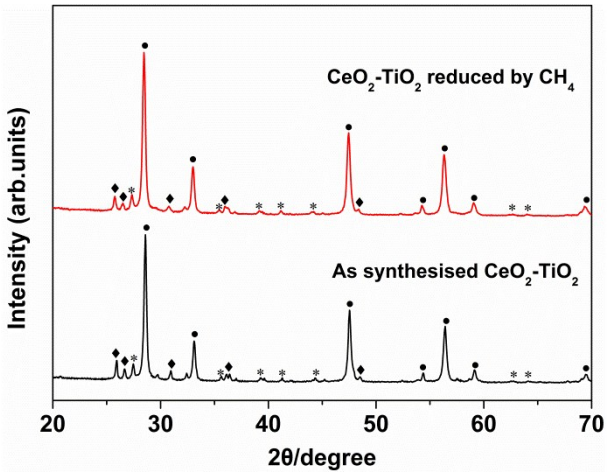

Fig. S7 X-ray powder diffraction patterns of as synthesized CeO_2-TiO_2 sample and CeO_2-TiO_2 sample after MDR step. Phases: (●)CeO_2, (*)TiO_2 (rutile), (◆)TiO_2 (brookite). The reduced sample after MDR step was cool down under flowing Ar and subjected to XRD measurement.

Fig. S7 shows the XRD patterns of the as prepared CeO_2-TiO_2 sample before and after MDR step. It is obvious that the as synthesized sample exhibited distinct reflection peaks corresponding to CeO_2 and TiO_2 (rutile, JCPDS 01-083-2242; brookite, JCPDS 01-076-1934). No apparent change in XRD patterns was observed for CeO_2-TiO_2 sample after MDR step, further confirming that negligible reduction of CeO_2 and TiO_2 occurred after reducing with CH_4.

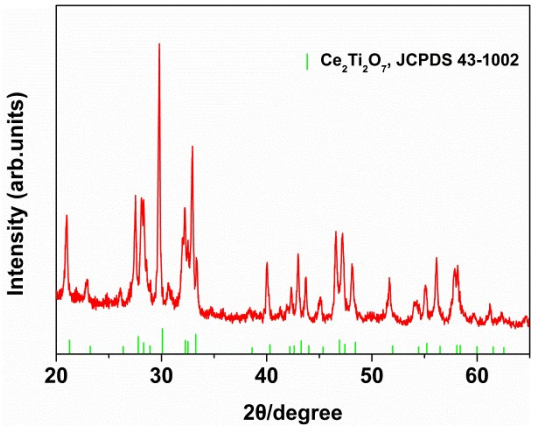

Fig. S8 X-ray powder diffraction pattern of CeO_2-TiO_2 sample after H_2-TPR measurement. The reduced sample after H_2-TPR experiment was cool down under flowing Ar and subjected to XRD measurement.

The XRD patterns of CeO_2-TiO_2 after H_2-TPR measurement clearly indicated the formation of $Ce_2Ti_2O_7$ pyrochlore (JCPDS 00-047-0667), which verified that a stoichiometric reaction between CeO_2 and TiO_2 occurred after reducing with H_2.

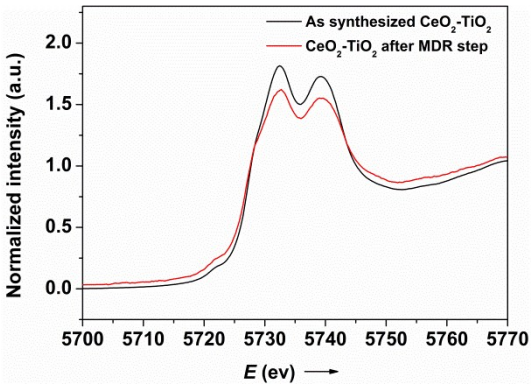

Fig. S9 Normalized XANES spectra for as synthesized CeO_2-TiO_2 sample and CeO_2-TiO_2 sample after MDR step at the Ce L_{III}-edge.

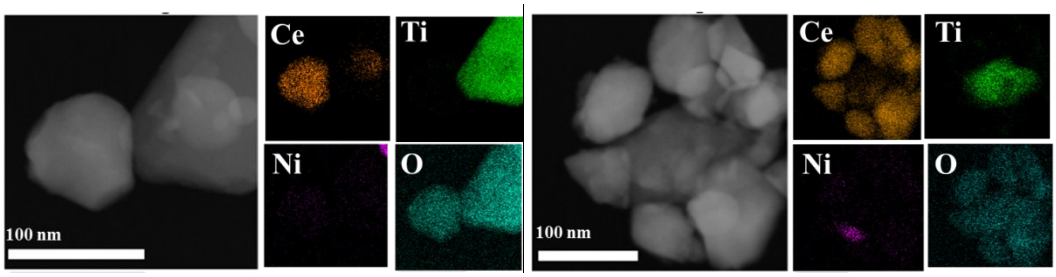

Fig. S10 STEM images and the according element-mapping images of Ce, Ti, Ni, and O for as synthesized 5Ni/CeO_2-TiO_2 in different regions.

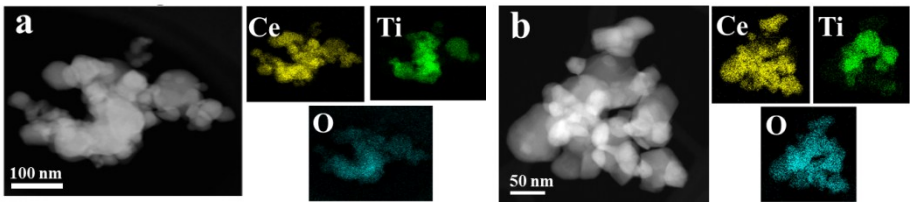

Fig. S11 (a) STEM image and the according element-mapping images of Ce, Ti, and O for as synthesized CeO_2-TiO_2 sample; (b) STEM image and the according element-mapping images of Ce, Ti, and O for CeO_2-TiO_2 sample after MDR step.

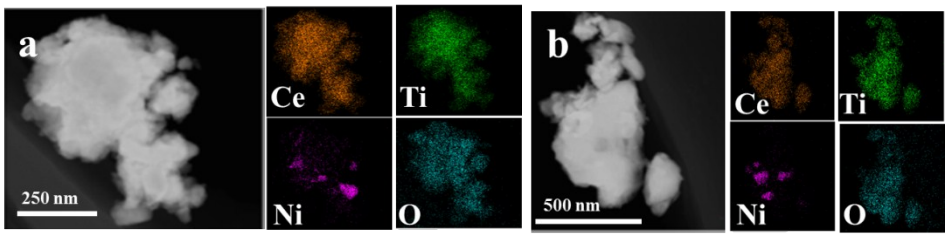

Fig. S12 (a) STEM image and the according element-mapping images of Ce, Ti, Ni, and O for 5Ni/CeO_2-TiO_2 after isothermal MDR-STCDS redox cycling at 900 ^oC; (b) STEM image and the according element-mapping images of Ce, Ti, Ni, and O for 5Ni/CeO_2-TiO_2 after isothermal MDR-STWS redox cycling at 900 ^oC.

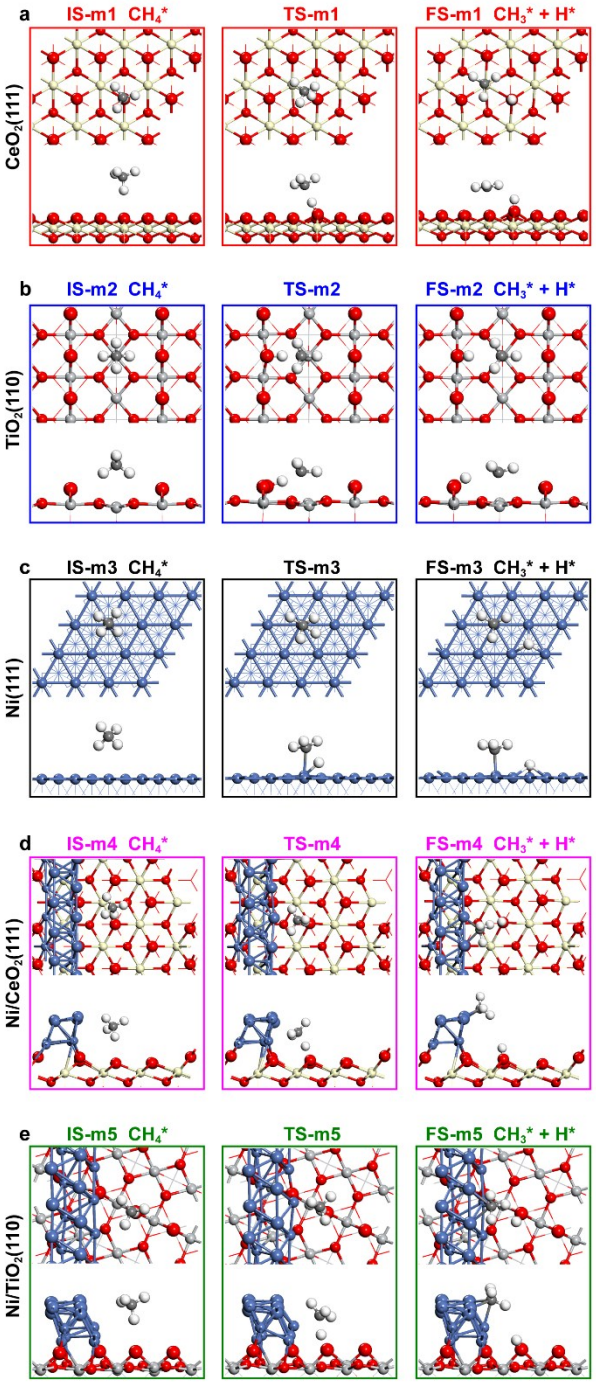

Fig. S13 Top (up) and side (down) view of states of methane dissociation ($CH_4(g) \rightarrow CH_3^* + H^*$) in Fig. 10(a).

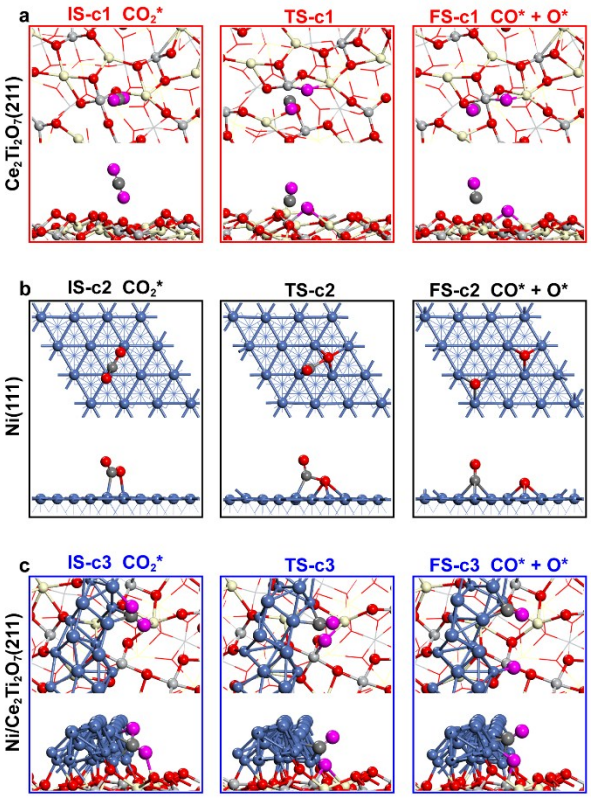

Fig. S14 Top (up) and side (down) view of states of CO_2 dissociation ($CO_2(g) \rightarrow CO^* + O^*$) in Fig. 10(b). The oxygen atoms from CO_2 are colored in magenta.

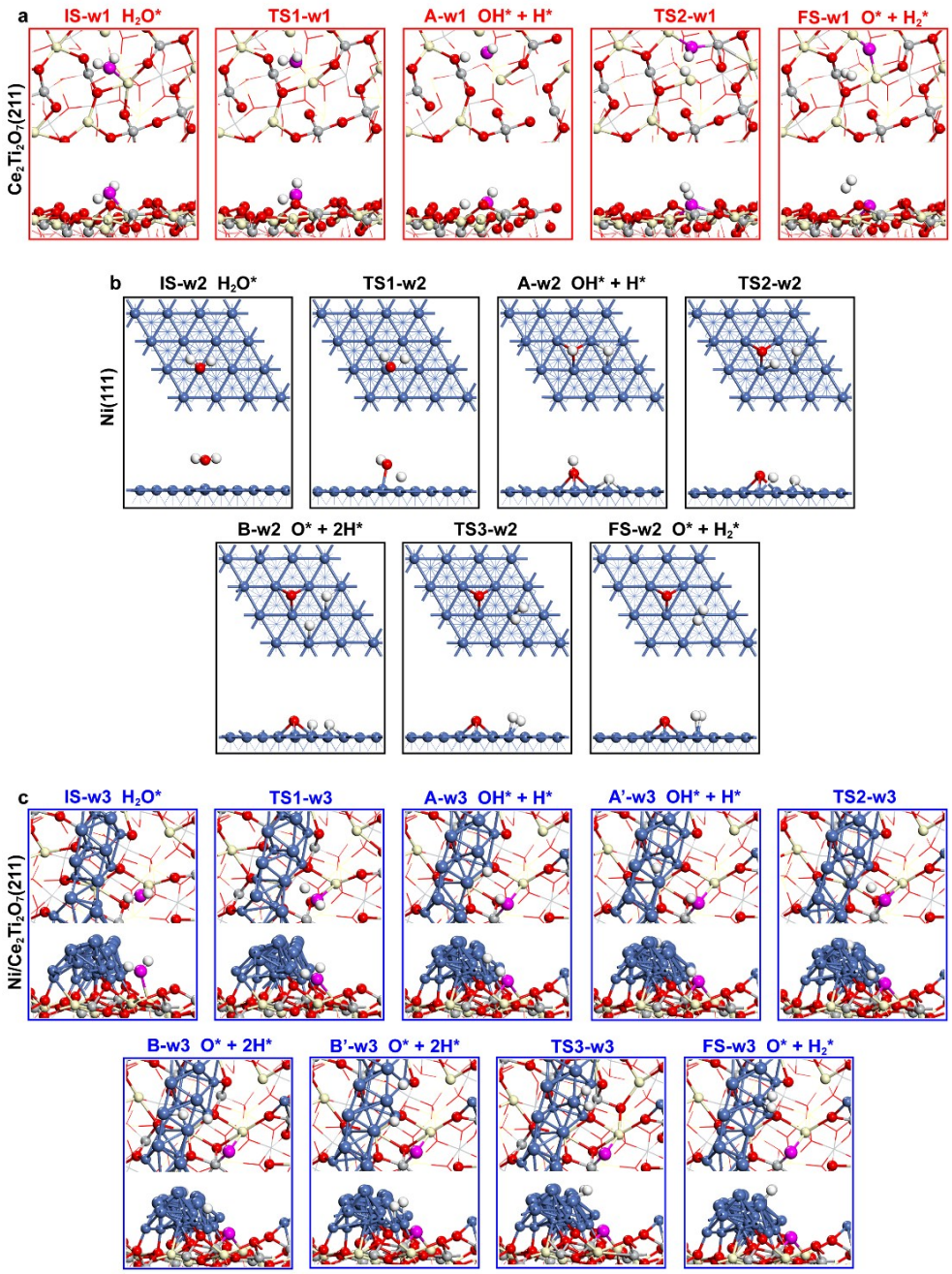

Fig. S15 Top (up) and side (down) view of states of H_2O splitting ($H_2O(g) \rightarrow O^* + H_2^*$) in Fig. 10(c). The oxygen atoms from H_2O are colored in magenta.

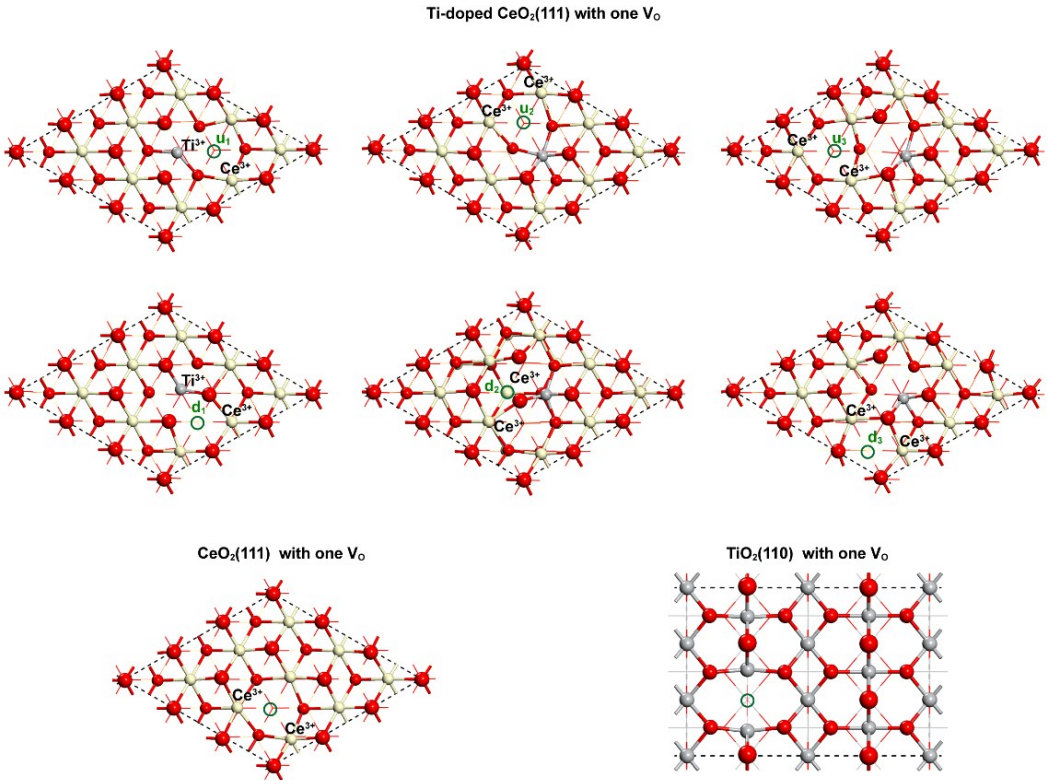

Fig. S16 Top views of oxide surface with one oxygen vacancy (V_O), corresponding to the oxygen vacancy listed in Fig. 10(d). The position of oxygen vacancy is labelled by a green circle.

Table S1. *k*-point meshes used for bulks and surfaces

	Models	*k*-points
Bulks	Ni	11 × 11 × 11
	CeO_2	7 × 7 × 7
	rutile TiO_2	4 × 4 × 7
	$Ce_2Ti_2O_7$	5 × 5 × 2
Surfaces	Ni(111)	3 × 3 × 1
	CeO_2(111)	1 × 1 × 1
	TiO_2(110)	1 × 1 × 1
	$Ce_2Ti_2O_7$(211)	1 × 1 × 1
	Ni/CeO_2(111)	1 × 2 × 1
	Ni/TiO_2(110)	1 × 2 × 1
	Ni/$Ce_2Ti_2O_7$(211)	1 × 1 × 1

Table S2. Optimized lattice constants of metal and metal oxides

Bulks	Lattice constant
Ni	$a = b = c = 3.479$ Å
CeO_2	$a = b = c = 5.428$ Å
rutile TiO_2	$a = b = 4.609$ Å, $c = 3.002$ Å
$Ce_2Ti_2O_7$	$a = 7.786$, $b = 5.428$ Å, $c = 13.055$ Å, $\beta = 98.59$ °

Table S3. Detailed structural parameters of slab models

Surface facets	Size of supercells	Number of atomic layers	Number of frozen layers	Vacuum space (Å)	Number of atoms
Ni(111)	p(3 × 3)	4	2	15	Ni 36
CeO_2(111)	p(3 × 3)	9	3	15	Ce 27 , O 54
TiO_2(110)	p(3 × 2)	6	3	15	Ti 24, O 48
$Ce_2Ti_2O_7$(211)	p(1 × 1)		half of the total atoms (Ce 8, Ti 8, O 28)	15	Ce 16, Ti 16, O 56
Ni/CeO_2(111)	p(4 × 2) for CeO_2(111)	6 for CeO_2(111), 2 for Ni nanorod	2 for CeO_2(111)	20	Ni 12, Ce 16, O 32
Ni/TiO_2(110)	($\sqrt{5}$ × $\sqrt{5}$)∠49.46° for TiO_2(110)	6 for TiO_2(110), 2 for Ni nanorod	3 for TiO_2(110)	20	Ni 12, Ti 16, O 32
Ni/$Ce_2Ti_2O_7$(211)	p(1 × 1) for $Ce_2Ti_2O_7$(211)	2 for Ni nanorod	half of the atoms (Ce 8, Ti 8, O 28) for $Ce_2Ti_2O_7$(211)	18	Ni 28, Ce 16, Ti 16, O 56

Table S4. Comparison of peak CO production rates and corresponding total CO yields for two-step STCDS, HDR-STCDS (H_2 driven reduction solar thermochemical CO_2 splitting) and MDR-STCDS processes

Redox material	**Temp (°C; red/ox)**	**Process**	**Sweep gas**	**Feed CO_2 (%)**	**Peak CO rate (mLmin^{-1} g^{-1})**	**Total CO yield (mL g^{-1})**	**Ref.**
CeO_2	1500/800	STCDS	Ar	50	10.0	6.9	Chueh *et al.*[1]
$Ce_{0.975}Zr_{0.025}O_2$	1400/800	STCDS	N_2	25	13.0	3.0	Gibbons *et al.*[2]
CeO_2	1250/850	STCDS	N_2	25	6.3	0.9	Rudisill *et al.*[3]
CeO_2	1400/800	STCDS	N_2	100	9.0	2.1	Malonzo *et al.*[4]
CeO_2	1500/1000	STCDS	Ar	38.5	—	2.1	Furler *et al.*[5]
$Sr_{0.4}La_{0.6}Mn_{0.6}Al_{0.4}O_{3-\delta}$	1350/1000	STCDS	He	40	1.3	6.6	McDaniel *et al.*[6]
CeO_2	1500/900	STCDS	Ar p_{total} =10mbar	—	1.2	6.3	Marxer *et al.*[7]
CeO_2-Fe_2O_3	600/600	HDR-STCDS	5%H_2/Ar	100	43.0	24.6	Galvita *et al.*[8]
CeO_2	900/900	HDR-STCDS	14.3%H_2/Ar	14.3	94.9	22.7	Zhao *et al.*[9]
$Ce_{0.5}Zr_{0.5}O_2$	900/900	HDR-STCDS	14.3%H_2/Ar	14.3	115.4	18.5	Zhao *et al.*[9]
$La_{0.6}Ca_{0.4}Fe_{0.4}Mn_{0.6}O_3$	550/950	HDR-STCDS	10%H_2/He	10	3.6	21.8	Maiti *et al.*[10]
$La_{0.75}Sr_{0.25}FeO_3/SiO_2$	600/600	HDR-STCDS	10%H_2/He	10	3.6	11.6	Hare *et at.*[11]
CeO_2-TiO_2	900/900	HDR-STCDS	1%H_2/Ar	100	33.4	40.7	This work
Fe_2TiO_5	1050/1050	MDR-STCDS	50%CH_4/N_2	10	1.7	—	Luo *et al.*[12]
CeO_2	1000/1000	MDR-STCDS	40%CH_4/Ar	40	28.6	—	Nair *et al.*[13]
$La_{0.6}Sr_{0.4}Co_{0.2}Fe_{0.8}O_{3-\delta}$	1029/1029	MDR-STCDS	100%CH_4	100	1.7	—	Michalsky *et al.*[14]
$Sr_3Fe_2O_{7-\delta}$-$Ca_{0.5}Mn_{0.5}O$	900/900	MDR-STCDS	10%CH_4/Ar	10	29.3	34.3	Zhang *et al.*[15]
5Ni/CeO_2-TiO_2	900/900	MDR-STCDS	1%CH_4/Ar	100	168.8	48.3	This work

Table S5. Comparison of peak H_2 production rates and corresponding total H_2 yields for two-step STWS, HDR-STWS (H_2 driven reduction solar thermochemical H_2O splitting) and MDR-STWS processes

Redox material	**Temp (°C; red/ox)**	**Process**	**Sweep gas**	**Feed H_2O (%)**	**Peak H_2 rate (mLmin^{-1} g^{-1})**	**Total H_2 yield (mL g^{-1})**	**Ref.**
CeO_2	1500/800	STWS	Ar	44-52	10.0	6.2	Chueh *et al.*[1]
CeO_2	1500/1150	STWS	N_2	50-80	5.6	10.2	Gokon *et al.*[16]
Rh/CeO_2	1500/1500	STWS	Ar	15	1.5	2.0	Hao *et al.*[17]
CeO_2-0.15SnO_2	1400/800	STWS	Ar	4.2	3.0	7.2	Ruan *et al.*[18]
$Ce_{0.75}Zr_{0.25}O_{2-\delta}$	1450/1045	STWS	He	—	0.47	5.3	Abanades *et al.*[19]
$CoFe_2O_4/Al_2O_3$	1350/1350	STWS	He	50	0.7	2.3	Muhich *et al.*[20]
$Co_{0.4}Fe_{0.6}Al_2O_4$	1500/1350	STWS	He	50	2.2	6.9	Muhich *et al.*[21]
$La_{0.8}Sr_{0.2}MnO_{3-\delta}$	1400/800	STWS	Ar	20	1.3	2.9	Yang *et al.*[22]
$Sr_{0.4}La_{0.6}Mn_{0.6}Al_{0.4}O_{3-\delta}$	1350/1000	STWS	He	40	1.7	6.9	McDaniel *et al.*[6]
Fe_2O_3/ZrO_2	600/600	HDR-STWS	H_2, CO, CO_2/He	5-6	49.7	17.8	Scheffe *et al.*[23]
$Co_{0.85}Fe_{2.15}O_4/ZrO_2$	600/600	HDR-STWS	H_2, CO, CO_2/He	5-6	53.9	92.5	Scheffe *et al.*[23]
$Ce_{0.8}Zr_{0.2}O_2$	825/825	HDR-STWS	5% H_2/Ar	2.7	17.9	26.4	Petkovich *et al.*[24]
CeO_2	700/700	HDR-STWS	14%H_2/Ar	26	80.6	5.8	Zhao *et al.*[25]
CeO_2-TiO_2	900/900	HDR-STWS	1%H_2/Ar	4.2	20.5	40.3	This work
$Fe_2O_3/Ce_{0.5}Zr_{0.5}O_2$	800/800	MDR-STWS	15%CH_4/He	—	15.7	—	Galvita *et al.*[26]
$La_{0.8}Sr_{0.2}FeO_{3-\delta}$-$Fe_3O_4$	900/750	MDR-STWS	10%CH_4/He	—	1.6	96.3	He *et al.*[27]
5Ni/CeO_2-TiO_2	900/900	MDR-STWS	1%CH_4/Ar	4.2	97.5	47.0	This work

Table S6. Reaction energies ΔE (eV) and activation energies E_a (eV) for the elementary steps involved in methane dissociation ($CH_4(g) \rightarrow CH_3^* + H^*$) on metal, oxide, and metal-oxide interface

reactions	$CeO_2(111)$		$TiO_2(110)$		Ni(111)		$Ni/CeO_2(111)$		$Ni/TiO_2(110)$	
	ΔE	E_a	ΔE	E_a	ΔE	E_a	ΔE	E_a	ΔE	E_a
$CH_4(g) \rightarrow CH_4^*$	–0.13		–0.35		–0.25		–0.30		–0.28	
$CH_4^* \rightarrow CH_3^* + H^*$	1.16	1.44	1.04	1.27	0.17	0.73	–0.86	0.80	–0.41	0.81

Table S7. Reaction energies ΔE (eV) and activation energies E_a (eV) for the elementary steps involved in carbon dioxide splitting ($CO_2(g) \rightarrow CO^* + O^*$) on metal, oxide, and metal-oxide interface

reactions	$Ce_2Ti_2O_7(211)$		Ni(111)		$Ni/Ce_2Ti_2O_7(211)$	
	ΔE	E_a	ΔE	E_a	ΔE	E_a
$CO_2(g) \rightarrow CO_2^*$	–0.49		–0.01		–0.82	
$CO_2^* \rightarrow CO^* + O^*$	1.08	1.45	–1.14	0.46	–1.89	0.82

Table S8. Reaction energies ΔE (eV) and activation energies E_a (eV) for the elementary steps involved in water splitting ($H_2O(g) \rightarrow H_2^* + O^*$) on metal, oxide, and metal-oxide interface[a]

reactions	$Ce_2Ti_2O_7(211)$		Ni(111)		$Ni/Ce_2Ti_2O_7(211)$	
	ΔE	E_a	ΔE	E_a	ΔE	E_a
$H_2O(g) \rightarrow H_2O^*$	–1.13		–0.50		–1.07	
$H_2O^* \rightarrow H^* + HO^*$	–0.10	0.34	–0.28	0.90	–1.72	1.13
$H^* + HO^* \rightarrow H_2^* + O^*$	2.99	3.53				
$H^* + HO^* \rightarrow 2H^* + O^*$			–0.09	1.09	0.64	1.03
$2H^* + O^* \rightarrow H_2^* + O^*$			0.62	0.68	0.51	0.80

[a] Two steps of hydrogen atom diffusion on $Ni/Ce_2Ti_2O_7(211)$ in Fig. 10c are not included here.

Table S9. The actual Ni loadings of the as-prepared catalysts determined by ICP-AES analysis

Sample	Ni (wt%)
5Ni/CeO_2-TiO_2	4.8
2Ni/CeO_2-TiO_2	1.9
1Ni/CeO_2-TiO_2	1.1
0.5Ni/CeO_2-TiO_2	0.5
CeO_2-TiO_2	-

Process mass balance on C, H, O:

Table S10. Summary of the integrated inlet and outlet gaseous species for 5Ni/CeO_2-TiO_2 redox catalyst during a typical reduction half cycle of MDR-STCDS and MDR-STWS processes

Process	**CH_4 inlet (mL/g)**	**CH_4 outlet (mL/g)**	**CH_4 converted (mL/g)**	**reduction products (mL/g)**					**O^{2-} extracted (mL/g)[c]**	**CH_4 Conversion**	**CO selectivity**
				CO	H_2	CO_2	H_2O[a]	C[b]			
MDR-STCDS	47.8	0.9	46.9	36.3	71.8	10.6	22.0	0	79.5	98.1%	77.4%
MDR-STWS	47.3	0.3	47.0	40.5	77.0	6.5	17.0	0	70.5	99.3%	86.1%

[a]The H_2O produced was removed by a condenser before entering the mass spectrometer, so the undetectable H_2O was calculated through mass balances between the converted CH_4 and measurable product gases.

[b]As no detectable amount of CO_2 or CO was observed during the H_2O splitting cycle, indicating the negligible carbon deposition after the CH_4 driven reduction step.

[c]The O^{2-} consumed during the reduction half cycle was derived from CeO_2-TiO_2 (44.5 mL/g), the loading NiO (19.1 mL/g), and the surface oxygen in hydroxyl and carbonate species, very close to the measure one.

References

1. W. C. Chueh, F. C., Abbott M., S. D., F. P., S. M. Haile and A. Steinfeld, *Science*, 2010, **330**, 1797-1801.
2. W. T. Gibbons, L. J. Venstrom, R. M. De Smith, J. H. Davidson and G. S. Jackson, *Phys. Chem. Chem. Phys.*, 2014, **16**, 14271-14280.
3. S. G. Rudisill, L. J. Venstrom, N. D. Petkovich, T. Quan, N. Hein, D. B. Boman, J. H. Davidson and A. Stein, *J. Phys. Chem. C*, 2013, **117**, 1692-1700.
4. C. D. Malonzo, R. M. De Smith, S. G. Rudisill, N. D. Petkovich, J. H. Davidson and A. Stein, *J. Phys. Chem. C*, 2014, **118**, 26172-26181.
5. P. Furler, J. Scheffe, D. Marxer, M. Gorbar, A. Bonk, U. Vogt and A. Steinfeld, *Phys. Chem. Chem. Phys.*, 2014, **16**, 10503-10511.
6. A. H. McDaniel, E. C. Miller, D. Arifin, A. Ambrosini, E. N. Coker, R. O'Hayre, W. C. Chueh and J. Tong, *Energy Environ. Sci.*, 2013, **6**, 2424.
7. D. Marxer, P. Furler, M. Takacs and A. Steinfeld, *Energy Environ. Sci.*, 2017, **10**, 1142-1149.
8. V. V. Galvita, H. Poelman, V. Bliznuk, C. Detavernier and G. B. Marin, *Ind. Eng. Chem. Res.*, 2013, **52**, 8416-8426.
9. Z. Zhao, M. Uddi, N. Tsvetkov, B. Yildiz and A. F. Ghoniem, *Phys. Chem. Chem. Phys.*, 2017, **19**, 25774-25785.
10. D. Maiti, B. J. Hare, Y. A. Daza, A. E. Ramos, J. N. Kuhn and V. R. Bhethanabotla, *Energy Environ. Sci.*, 2018, **11**, 648-659.
11. B. J. Hare, D. Maiti, Y. A. Daza, V. R. Bhethanabotla and J. N. Kuhn, *ACS Catal.*, 2018, **8**, 3021-3029.
12. S. Luo, L. Zeng, D. Xu, M. Kathe, E. Chung, N. Deshpande, L. Qin, A. Majumder, T.-L. Hsieh, A. Tong, Z. Sun and L.-S. Fan, *Energy Environ. Sci.*, 2014, **7**, 4104-4117.
13. M. M. Nair and S. Abanades, *Energy Fuels*, 2016, **30**, 6050-6058.
14. R. Michalsky, D. Neuhaus and A. Steinfeld, *Energy Technol.*, 2015, **3**, 784-789.
15. J. Zhang, V. Haribal and F. Li, *Sci. Adv.*, 2017, **3**, e1701184.
16. N. Gokon, T. Suda and T. Kodama, *Thermochim. Acta*, 2015, **617**, 179-190.
17. Y. Hao, C.-K. Yang and S. M. Haile, *Chem. Mater.*, 2014, **26**, 6073-6082.
18. C. Ruan, Y. Tan, L. Li, J. Wang, X. Liu and X. Wang, *AIChE J.*, 2017, **63**, 3450-3462.
19. S. Abanades, A. Legal, A. Cordier, G. Peraudeau, G. Flamant and A. Julbe, *J. Mater. Sci.*, 2010, **45**, 4163-4173.
20. C. L. Muhich, B. W. Evanko, K. C. Weston, P. Lichty, X. Liang, J. Martinek, C. B. Musgrave and A. W. Weimer, *Science*, 2013, **341**, 540-542.
21. C. L. Muhich, B. D. Ehrhart, V. A. Witte, S. L. Miller, E. N. Coker, C. B. Musgrave and A. W. Weimer, *Energy Environ. Sci.*, 2015, **8**, 3687-3699.
22. C.-K. Yang, Y. Yamazaki, A. Aydin and S. M. Haile, *J. Mater. Chem. A*, 2014, **2**, 13612.
23. J. R. Scheffe, M. D. Allendorf, E. N. Coker, B. W. Jacobs, A. H. McDaniel and A. W. Weimer, *Chem. Mater.*, 2011, **23**, 2030-2038.
24. N. D. Petkovich, S. G. Rudisill, L. J. Venstrom, D. B. Boman, J. H. Davidson and A. Stein, *J. Phys. Chem. C*, 2011, **115**, 21022-21033.
25. Z. Zhao, M. Uddi, N. Tsvetkov, B. Yildiz and A. F. Ghoniem, *J. Phys. Chem. C*, 2016, **120**, 16271-16289.
26. V. Galvita and K. Sundmacher, *Appl. Catal. A*, 2005, **289**, 121-127.
27. F. He, J. Trainham, G. Parsons, J. S. Newman and F. Li, *Energy Environ. Sci.*, 2014, **7**, 2033-2042.